EFFECTS OF REYNOLDS NUMBER, MACH NUMBER AND STING GEOMETRY ON ROTARY BALANCE MEASUREMENTS

by

C. O. O'Leary
B. Weir

Royal Aerospace Establishment
Bedford MK41 6AE, UK

Abstract

Although extensive assessments of the effects of Reynolds number, Mach number and sting geometry have been made for static tests there have been few similar studies for rotary tests. This paper describes the results of exploratory tests on the RAE HIRM 1 and HIRM 2 models. Effects on the lateral coefficients are assessed. Test Reynolds number and Mach number ranges were 0.7×10^6 to 3.8×10^6 and 0.2 to 0.8 respectively. Results showed that asymmetric forces could be generated, depending on Reynolds number and rate of roll. Reynolds number also affected the linearity and magnitude of sideforce, yawing moment and rolling moment due to rate of roll. Effects of rear sting geometry were most prominent at $\alpha = 40°$. A dummy top-entry sting caused most interference to C_y and C_n at $\alpha = 40°$ and 60° but effects on C_l were confined to $\alpha = 40°$. There was a reduction in roll damping for Mach number increases between 0.4 and 0.8.

1. Introduction

During vigorous manoeuvring and spinning, combat aircraft may be subjected to high rates of rotation. To study flow behaviour and forces acting on the aircraft under these conditions, models are tested on a rotary balance. In recent years rotary balances have been developed in several test centres and there is considerable interest in the application of this test technique to provide information on the aerodynamics of rotary flows. An AGARD Working Group has recently completed a three year study of the subject.

Rotary balance tests are invariably made at Reynolds numbers well below full scale values and, as in conventional static tests, there are likely to be scale effects. The nature of these effects will depend on various factors including model and support configuration, angle-of-attack and rotation rate. Effects of Reynolds number have been well researched for static tests but this is not the case for rotary tests where the basic measurement of forces and moments has been a fairly challenging task. Previous tests on the RAE High Incidence Research Models, HIRM 1[1] and HIRM 2[2], showed that there were significant Reynolds number effects on rotary balance data at particular angles-of-attack. Tests by Malcolm[3] on an F-15 model also showed that, at high angles-of-attack, yawing moment (referenced to body axes) was particularly dependent on Reynolds number but the magnitude and nature of the effect varied with model configuration and sting geometry. Results presented in this paper show, at low speed, the effects of Reynolds number on lateral forces and moments for HIRM 1 and HIRM 2.

Model support interference has also been investigated in static tests but there have been few attempts to measure these effects in rotary tests even though there are usually more substantial structural components relatively near the model which are likely to cause significant interference. The pressure field near the model will be modified by the presence of support components and on some models there may be premature breakdown of wing vortices or modification of forebody vortices. A particular problem is interference from a top-entry sting which is the type of model support usually used for rotary tests at high angles-of-attack. To investigate these effects low speed tests were made on HIRM 2: a) with two rear-entry stings of different geometry at angles-of-attack up to 40° and b) with and without a dummy top-entry sting at angles-of-attack up to 60°.

Most rotary tests are made at low speed because of the requirement for data relating to the study of spinning characteristics of combat aircraft. However, there is also interest in the application of rotary balance data to the mathematical modelling of manoeuvring flight at high subsonic Mach number. It is therefore necessary to test at these higher speeds to assess the significance of Mach number effects. Results for HIRM 1[1] indicated that these effects were not very significant but tests on another configuration[4] showed considerable variation in measured forces due to Mach number. In the present tests, measurements were made on HIRM 2 in the range $M = 0.2$ to $M = 0.8$, at angles-of-attack of 16° and 24°.

The various tests reported in this paper were undertaken as a preliminary investigation only. It is hoped to explore the most significant effects in future, more comprehensive, tests.

2. Description of Rotary Balance and Models

The RAE Rotary Balance, shown in Fig 1, is fully described elsewhere[1] so only brief details will be given here. The model is mounted on a five-component strain-gauge balance and can be rotated at speeds up to 400 rpm at angles-of-attack up to 60°. Balance signals are taken out through slip rings at the rear of the drive shaft. The rig is powered by a servo-controlled hydraulic motor supplied by a pump unit located outside the wind-tunnel working section. Two cranked stings are available: one for tests at angles-of-attack up to 40° and another for tests in the range $8° < \alpha < 60°$. Angle-of-attack has to be changed manually by bolting and clamping the sting in the desired setting on the rotor. Balance weights, fitted on carriers at the ends of the rotor, are adjusted for each

angle-of-attack setting. Strain gauge balance signals are processed on-line to eliminate balance interactions and gravity and inertial components.

When testing with the 60° crank sting, aerodynamic interference from a top-entry sting could be simulated by fitting a dummy as shown in Fig 1. The position of the dummy relative to the model could be maintained constant when changing the angle-of-attack of the rear sting. There was adequate clearance between the end of the dummy and the model to prevent contact when the model deflected under load.

General arrangements of HIRM 1 and HIRM 2 are shown in Figs 2&3 and leading particulars are given in Table 1. Both configurations have been the subjects of an extensive RAE investigation into the characteristics of combat aircraft at high angles-of-attack. HIRM 1 is a three surface configuration having a 42° swept wing, with leading edge droop for the present tests. Tailplanes and forplanes were set at -20° and -10° respectively. HIRM 2 is typical of a delta-canard agile fighter with a wing leading edge swept at 58° and leading edge camber appropriate to fight at high angle-of-attack. Flaps and foreplanes were set to zero. The models are made mainly from aluminium alloy with their centres of gravity very close to the balance axis to minimise inertial loads. 'Heavy metal' balancing weights are used to achieve this. The total mass of each model is approximately 15 kg.

3. Tests

Tests were made in the 4m x 2.7m Atmospheric Wind Tunnel at RAE Bedford and in the 2.4m x 1.8m Variable Density Wind Tunnel at RAE Farnborough. The test procedure for the two tunnels was similar except that when testing at high speeds in the Farnborough tunnel it was necessary to do a warm-up run prior to taking data to minimise drifts on the balance. For each configuration and angle-of-attack the model was rotated, wind-off and wind-on, at a series of positive and negative speeds up to 350 rpm. After each set of runs the differences between wind-on and wind-off data were processed to obtain the force and moment coefficients. Corrections were made for measured drifts of the balance zeros. To include the wind-off damping components in the aerodynamic measurements, the mean of the wind-off measurements at equal positive and negative rotation rates was subtracted from the wind-on data. This procedure is appropriate for symmetrical configurations because the sign of the wind-off damping is always equal and opposite to the direction of rotation. Details of all tests are given in Table 2.

For some low-speed tests in the Bedford tunnel, flow on the model was visualized using minitufts[5]. These are very fine pieces of nylon monofilment (0.04mm diameter) which are fixed to the surface of the model but cause very little interference. The tufts are coated with fluorescent dye and when the model is photographed in ultra-violet light a clear picture of the flow pattern on the model is obtained. Still photographs were taken by synchronizing the operation of flash guns and camera, situated behind a clear panel in the roof of the working-section, with rotational position of the model. In these tests flow patterns on the wing upper surface were studied.

4. Results and Discussion

Although the models were rotated about a wind axis, results presented in this section are coefficients in body axes. In the authors' opinion, data referred to body axes give a better indication of the source of the measured differences. Coefficients are plotted against non-dimensional rotation rate $\Omega b/2V$, where Ω is the rate of rotation about the wind tunnel axis. Only lateral coefficients are presented and discussed.

4.1 Reynolds number effects

For HIRM 1, the effects on C_n and C_l vs $\Omega b/2V$ of doubling the Reynolds number from 1.4×10^6 to 2.8×10^6 are shown in Figs 4a, 4b&4c for angles-of-attack of 16°, 22° and 36° respectively. At $\alpha = 16°$ (Fig 4a), there is linear variation of damping for both C_n and C_l and small effect of Reynolds number, only just detectable with the limited number of rotation speeds. At $\alpha = 22°$ (Fig 4b), damping has diminished and become non-linear, especially in the case of rolling moment, but the effect of Reynolds number remains small. At $\alpha = 36°$ (Fig 4c) however, results from two separate runs at each Reynolds number show that there is an apparent Reynolds number effect. C_n varies linearly with roll rate at both Reynolds numbers but there is a negative offset at all values of $\Omega b/2V$ at the higher Reynolds number. A more significant difference is apparent in the variation of C_l where an increase in Reynolds number results in a large positive rolling moment at zero roll rate which diminishes as $|\Omega b/2V|$ increases beyond 0.1. At the lower Reynolds number C_l is small at all roll rates.

Flow visualization on the upper surfaces of the wings for $\Omega b/2V = 0.04$, $\alpha = 16°$, 22° and 36° are shown in Figs 5a, 5b&5c respectively. These photographs were taken in the 4m x 2.7m Wind Tunnel at $Re = 1.4 \times 10^6$ but were, unfortunately, not repeated in the 2.4m x 1.8m Pressurised Wind Tunnel at $Re = 2.8 \times 10^6$. However, they do give some indication of the behaviour of the flow as angle-of-attack is increased. At moderate angle-of-attack (Fig 5a) the induced differential angle-of-attack on the outboard port and starboard wings causes an asymmetric flow pattern, with evidence of a vortex on the outer starboard wing and consequent increased suction. The model is damped in roll at this angle-of-attack, as shown in Fig 4a. At $\alpha = 22°$ however, the tufts indicate a burst vortex over the starboard wing due to increased angle-of-attack, whereas vortex flow appears to be re-established on the port outer wing (Fig 5b). Thus damping would be reduced as shown in Fig 4b. The change in Reynolds number apparently has little effect on these flow mechanisms. At $\alpha = 36°$ (Fig 5c) the flow on both wings is complex but symmetric and generates little differential lift at $Re = 1.4 \times 10^6$, as indicated by the small and variable rolling

moments shown in Fig 4c. Previous static tests[6] on the HIRM 1 configuration showed that at high angles-of-attack forebody vortices can become asymmetric and tests on another model[7] indicated that there is a critical Reynolds number, near those for the present tests, at which this phenomena is triggered. As suggested by Ericsson[8], asymmetric forebody vortices may interact with the wing/foreplane flow to generate the rolling and yawing moments at $Re = 2.8 \times 10^6$ (Fig 4c).

Effects of Reynolds number on C_n and C_l for HIRM 2 are shown in Figs 6a to d for four angles-of-attack between 20° and 60°. For $\alpha = 20°$, tests were made at $Re = 1.3$ and 3.8×10^6 but for $\alpha = 40°$, 50° and 60° the model was also tested at $Re = 0.7 \times 10^6$.

At $\alpha = 20°$ (Fig 6a) Cn and C_l vary linearly with $\Omega b/2V$ and Reynolds number has little effect. Similar results were obtained for $\alpha = 10°$, 16° and 28°. For this configuration, it may be expected that wing and foreplane vortices would maintain lift over most of the wing surface up to $\alpha \simeq 28°$ resulting in the linear variations of C_n and C_l shown in Fig 6a. With coherent vortex flow sensitivity to Reynolds number would not be expected. At $\alpha = 40°$, however, (Fig 6b) there are prominent non-linearities and differences due to Reynolds number. For positive rotation there is some reduction in the gradient of C_n but the effects on C_l are perhaps more significant. At low rotation rate the gradient increases negatively with increase in Reynolds number to 3.8×10^6 but at higher $\Omega b/2V$ this trend is reversed. It is probable that wing vortices have burst but the foreplane wake maintains some lift over the inboard wing. Forebody vortices may also interact to create a complex mixed flow over the model. When angle-of-attack is increased to this level, it is likely that the fin loading has less significance on C_n and then forebody flows have a dominant influence. On HIRM 2 however, there was no indication of large asymmetric yawing or rolling moment at higher Reynolds number for $\alpha \simeq 40°$.

When angle-of-attack is increased to 50° (Fig 6c), there is again a decrease in the gradient of C_n for $Re = 3.8 \times 10^6$, especially at low rotation rate. Damping in roll, C_l is virtually zero for $Re = 0.7$ and 1.3×10^6 but for $Re = 3.8 \times 10^6$, $|\Omega b/2V| < 0.2$ there is some damping. There is very little differential lift on the wing upper surfaces but some roll damping is generated by differential pressure on the wing lower surfaces at low rotation rate and $Re = 3.8 \times 10^6$.

At $\alpha = 60°$ (Fig 6d), there are large reductions in C_n with increase in Reynolds number but the effect on C_l is insignificant. Effects on C_n are probably due to Reynolds number sensitivity of the crossflow over the forward fuselage, which is of circular cross-section. A laminar crossflow at a low Reynolds number may generate significantly different forces on the nose compared to a crossflow with a turbulent boundary layer at a higher Reynolds number.

4.2 Effect of sting geometry

Two sets of results are compared. Firstly, results from tests with two rear sting cranks, the '40° crank' and the '60° crank', where the designation refers to the maximum test angle-of-attack; secondly, results from tests with and without a dummy top-entry sting. All the tests were made at $M = 0.2$, $Re = 1.3 \times 10^6$. It should be noted that changes in Mach number and/or Reynolds number may modify the measured effects.

4.2.1 Effect of rear sting crank

Effects on C_y and C_n for $\alpha = 20°$, 28° and 40° are shown in Figs 7a&7b. At $\alpha = 20°$ the variation of both coefficients with angular rate is linear. Differences due to crank shape are small, even though the geometry of the 60° crank is such that there is substantial flow disturbance immediately downstream of the fin of the model at this angle-of-attack. At $\alpha = 28°$ there is some effect on C_y, an increase of sideforce with the 60° crank, but, surprisingly, no effect on yawing moment. This could be explained by a forward movement in sideforce centre of pressure or by reduced differential suction on the cambered wing leading edges. At $\alpha = 40°$ substantial non-linearities appear and there are significant differences due to crank shape. As for results at $\alpha = 28°$, C_y increases more positively with $\Omega b/2V$ when the 60° crank is used but, at $\alpha = 40°$, the slope of C_n is less negative, except at very low rate of roll where there is no difference between the measurements. The effects of sting crank on rolling moment, C_l are shown in Fig 7c. Again, the effect is insignificant at $\alpha = 20°$ and more apparent at $\alpha = 28°$, where the 60° crank acts to increase the measured roll damping. However, at $\alpha = 40°$ there are very large differences between the two sets of data. With either crank the gradient changes from positive (negative damping) to negative as roll rate increases, but with the 60° crank the magnitude of C_l is much greater at the highest roll rates. The results show that at high angle-of-attack, $\alpha \simeq 40°$, rear sting geometry has a significant effect on the variation of C_y, C_n and C_l due to rate of roll. It is probable that the vortices from foreplane, wing and forebody interact to a greater extent with the 60° crank, increasing sideforce and rolling moment but decreasing yawing moment due to angular rate. However, as angle-of-attack increases beyond 40° there may be less effect with the 60° crank since it will then be further removed from the wake of the model.

4.2.2 Effect of dummy top-entry sting

Results for C_y and C_n vs $\Omega b/2V$, with and without a dummy top-entry sting (illustrated in Fig 1), for $\alpha = 40°$, 50° and 60° are shown in Figs 8a&8b. A top-entry sting would not normally be used for testing at low and moderate angles-of-attack. For $\alpha = 40°$, $\Omega b/2V > 0.05$, there is a significant reduction in the magnitude of C_y, with changes of sign due to the non-linear behaviour, and an increase in the magnitude of C_n with the dummy fitted. At $\alpha = 50°$ the dummy has only a small effect on C_y and C_n. At $\alpha = 60°$, however the effect of the dummy is

again significant. For negative rates of roll there are large positive increments in sideforce and yawing moment due to dummy, but for positive roll rates there is much less effect. At $\alpha = 40°$ (Fig 8c), the dummy has a marked effect on rolling moment, but at $\alpha = 50°$ and 60° the effects are negligible.

Since the measurements of C_y and C_n show substantial differences with the dummy on and off at 40° and 60° but little difference at $\alpha = 50°$ it is clear that interference effects are complex and could be a function of several factors, including model configuration, top-entry sting geometry and angle-of-attack. Effects on sideforce and yawing moment are probably due to interaction between forebody vortices and the dummy sting, with perhaps some interaction between the wake of the dummy sting and the fin. At $\alpha = 40°$ there is interference with the wing flow field which affects rolling moment, but as angle-of-attack is increased and the wing upper surface flow becomes totally separated and incoherent, the effect on C_l is diminished until at $\alpha = 60°$ there is no effect at all.

4.3 Mach number effects

C_y, C_n and C_l from tests on HIRM 2 are shown in Figs 9a, 9b&9c respectively for $\alpha = 16°$ and $\alpha = 24°$. Reynolds number for these tests was 1.3×10^6. Since maximum rotation was limited to 350 rpm, maximum test values of $\Omega b/2V$ reduced with increasing Mach number from 0.15 at $M = 0.2$ to 0.04 at $M = 0.8$. At each test Mach number, data were taken at eighteen rotation speeds but, for clarity, actual symbols have been omitted from the figures. The mean gradients over the range of $\Omega b/2V = \pm 0.04$ are shown as the derivatives $C_{y\Omega}$, $C_{n\Omega}$, and $C_{l\Omega}$ in Fig 10.

At $\alpha = 16°$ the gradient of C_y is fairly linear and positive at all test Mach numbers as shown in Fig 9a. For a positive rate of roll, a port to starboard sidewash is established on the model due to lower pressure over the starboard wing. This generates a positive sideforce on the fuselage and fin. Also, as angle-of-attack increases, the forward fuselage and the rear fuselage/fin are displaced from the axis of rotation and the measurements show that the sum of these sideforces is positive. The gradient of C_y vs $\Omega b/2V$, $C_{y\Omega}$, decreases with increasing Mach number as shown in Fig 10. The gradient of C_n is also substantially linear and negative at all Mach numbers (Fig 9b) but, as shown in Fig 10, the magnitude of $C_{n\Omega}$ reduces with Mach number. The relative signs of $C_{y\Omega}$ and $C_{n\Omega}$ indicate that the resultant total sideforce acts aft of the Moment Reference Centre. An additional contribution to yawing moment, which does not generate significant sideforce, may be from differential suction on the cambered wing leading edges. A positive rate of roll would normally generate a negative yawing moment, and it seems plausible that this differential suction would decrease with increasing Mach number.

When angle-of-attack is increased to 24°, the results in Figs 9a&9b show that linear variation of C_y and C_n is maintained. As for $\alpha = 16°$, there is a reduction in $C_{y\Omega}$ with Mach number but at $\alpha = 24°$ there is a slight increase in $|C_{n\Omega}|$ at $M = 0.8$ (Fig 10). These different effects of Mach number on $C_{n\Omega}$ at $\alpha = 16°$ and $\alpha = 24°$ remain unexplained.

For rolling moment, the results in Fig 9c show that there is substantially linear damping in roll up to $M = 0.8$, but at both test angles-of-attack there is a reduction in magnitude of $C_{l\Omega}$ as Mach number increases from 0.4 to 0.8 (Fig 10). For the HIRM 2 wing, static test results show that there is a small increase in lift slope between $M = 0.6$ and 0.8 at moderate angle-of-attack but results from the present tests indicate that even at $\alpha = 16°$, compressibility effects tend to reduce induced lift on the outboard wing (starboard for positive Ω) as Mach number increases beyond $M = 0.4$.

5 Conclusions

Rotary balance tests have been made to investigate the effects of Reynolds number, sting geometry and Mach number on sideforce, yawing moment and rolling moment due to rate of roll. Results are summarised as follows.

1 The main effects of Reynolds number were:

a. On HIRM 1 an increase in Reynolds number from 1.4×10^6 to 2.8×10^6 caused asymmetric yawing and rolling moments at high angle of attack ($\alpha = 36°$). These asymmetric moments tended to decrease at high roll rate.

b. On HIRM 2 there were significant effects of Reynolds number in the range $40° < \alpha < 60°$. At $\alpha = 40°$ and 50° an increase in Reynolds number from 0.7×10^6 to 3.8×10^6 had a significant effect on the variations of C_n and C_l vs $\Omega b/2V$. At $\alpha = 60°$ there were substantial effects on C_n but C_l was insensitive to Reynolds number.

2 Results of tests with two rear sting cranks of different geometry showed that there were only small effects on C_y and C_l at $\alpha = 20°$ and 28° but at $\alpha = 40°$ there were marked differences in the magnitude and gradient of C_y, C_n and C_l variation with roll rate.

3 The presence of a dummy top-entry sting caused marked changes in sideforce due to rate of roll at $\alpha = 40°$ and $\alpha = 60°$ but not at $\alpha = 50°$. Dummy sting effects on rolling moment were very prominent at $\alpha = 40°$ but were insignificant at $\alpha = 50°$ and 60°.

Sensitivity of wing and body vortices to Reynolds number and the interaction of these vortices with sting components is suggested as the probable cause of the most prominent measured effects on the lateral coefficients. These effects are complex and vary with angle-of-attack in the range $40° < \alpha < 60°$.

4 Effects of Mach number were measured on HIRM 2 at $\alpha = 16°$ and 24°. At both angles-of-attack variation of coefficients with roll rate was fairly linear up to the maximum test values of $\Omega b/2V$. There was a reduction in the gradient of C_l, $(C_{l\Omega})$ with increasing Mach number.

6 Future Tests

Low speed and high subsonic speed tests are currently being made on another advanced combat aircraft model providing more data on the effects of Reynolds number and Mach number. Plans are in hand to install a video camera on the rotating rig and obtain continuous visualization of the minitufts. This should help in understanding the complex flows indicated by force measurements.

An international collaborative programme of work is planned to investigate various aspects of rotary tests, including support interference and tunnel constraint effects.

TABLE 1 LEADING PARTICULARS OF MODELS

	HIRM 1	HIRM 2
Wing area, S	0.1018×10^6	0.1343×10^6 mm^2
Wing span, b	578.6	555.5 mm
Aerodynamic mean chord, $\bar{\bar{c}}$	192.9	279.8 mm
Moment Reference Centre	$0.125\ \bar{\bar{c}}$	$0.245\ \bar{\bar{c}}$

TABLE 2 TEST CONDITIONS

Model	Wind-tunnel	Speed	Reynolds No	Sting	Angles-of-attack
HIRM 1	2.4m x 1.8m	70 m/s	1.4×10^6	40 deg	16°, 22°, 36°
			2.8×10^6		
HIRM 2	4m x 2.7m	70 m/s	1.3×10^6	40 deg	20°, 28°, 40°
				60 deg	20°, 28°, 40°
	4m x 2.7m	70 m/s	1.3×10^6	60 deg	40°, 50°, 60°
				60 deg + dummy sting	40°, 50°, 60°
		35 m/s	0.7×10^6	60 deg	40°, 50°, 60°
	2.4m x 1.8m	70 m/s	1.3×10^6	60 deg	20°, 40°, 50°, 60°
			3.8×10^6	60 deg	20°, 40°, 50°, 60°
	2.4m x 1.8m	M = 0.2	1.3×10^6	40 deg	16°, 24°
		M = 0.4			
		M = 0.6			
		M = 0.8			

List of Symbols

b wing span

$\bar{\bar{c}}$ aerodynamic mean chord
C_l rolling moment coefficient
C_n yawing moment coefficient
C_y sideforce coefficient
M Mach number
Re Reynolds number
S reference wing area
V freestream velocity

α angle-of-attack
Ω rate of rotation about wind-tunnel axis

References

1 C.O. O'Leary, E.N. Rowthorn, New rotary rig at RAE and experiments on HIRM. RAE Technical Memorandum Aero 2039 (1985)

2 C.O.O'Leary, E.N. Rowthorn, Low speed dynamic tests on a canard configured high incidence research model (HIRM 2). RAE Technical Report 88024 (1988)

3 G.N. Malcolm, L.B. Schiff, Recent developments in rotary balance testing of fighter aircraft configurations at AMES Research Center. AGARD-CP-386 (1985)

4 R.P. Bennett, A. Watson, Multi-Facility Rolling Derivatives Rig. Part 3. Wind Tunnel Trials. BAe Report No AXR 60 Pt 3

5 C.O. O'Leary, W. Drew, Flow visualization on rolling models using minitufts. RAE Technical Memorandum Aero 2083

6. A. Jean Ross, G.E.A. Reid, The development of mathematical models for a high incidence research model. Part 1 Analysis of static aerodynamic data. RAE Technical Report 83037 (1983)

7 J.J. Brownson, R.E. Graham, D. Banducci, Static stability characteristics of Manned Spacecraft Center Straight-Wing Space Shuttle Orbiter: Effect of Reynolds number and body corner radius at M = 0.5. NASA TMX-62054, (1971)

8 L.E. Ericsson, Reflections regarding recent rotary rig results. Journal of Aircraft Vol. 24, No 1, (1987)

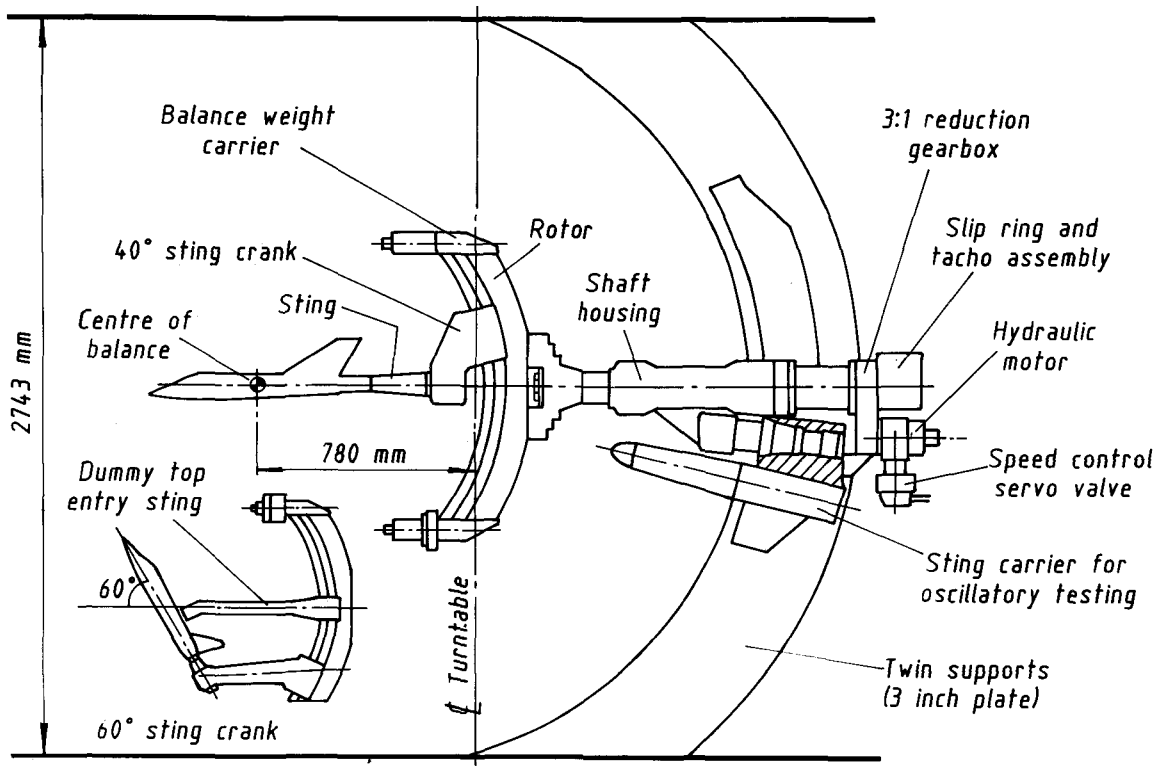

Fig 1 RAE rotary balance in 4 m x 2.7 m Wind Tunnel

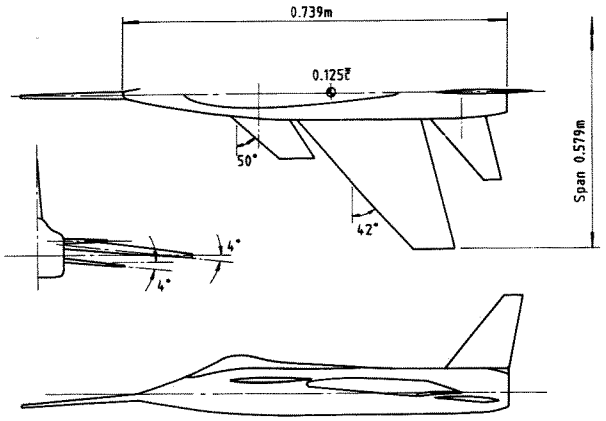

Fig 2 General arrangement of HIRM 1

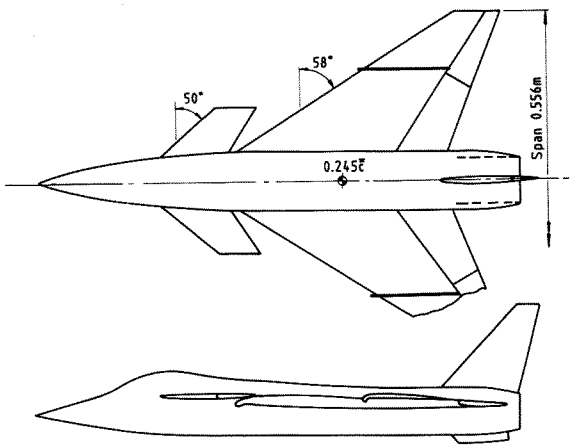

Fig 3 General arrangement of HIRM 2

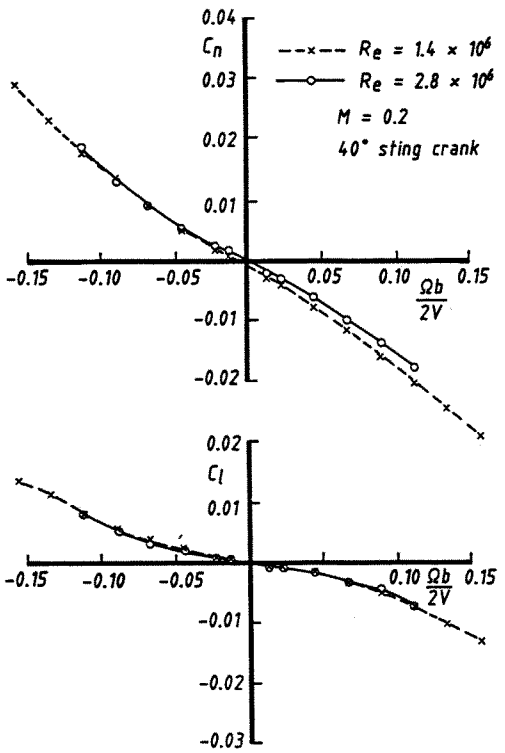

Fig 4b Reynolds number effects on C_n and C_ℓ. HIRM 1, α = 22°

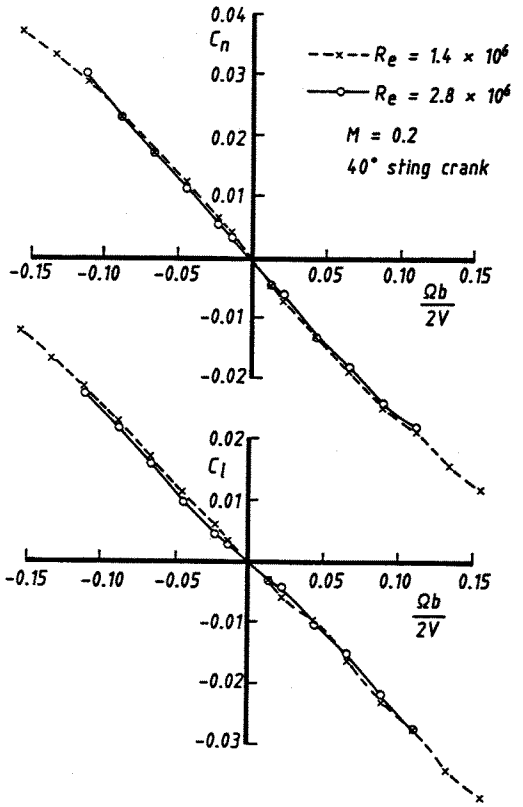

Fig 4a Reynolds number effects on C_n and C_ℓ. HIRM 1, α = 16°

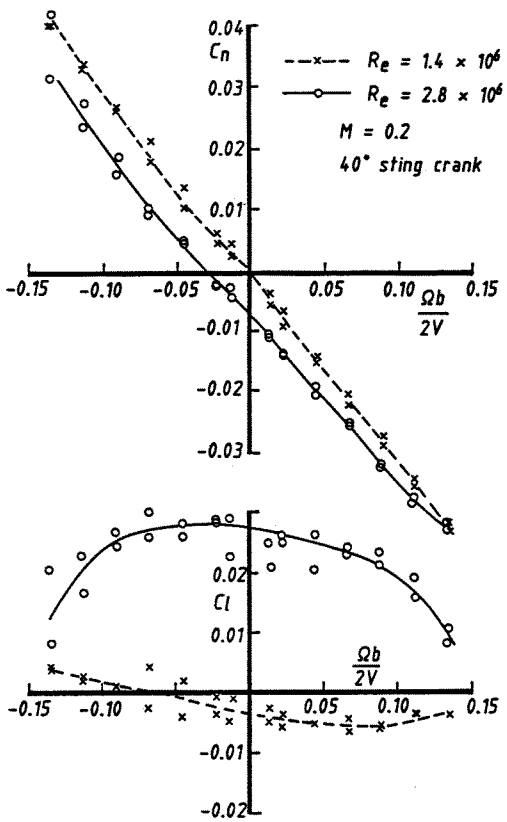

Fig 4c Reynolds number effects on C_n and C_ℓ. HIRM 1, α = 36°

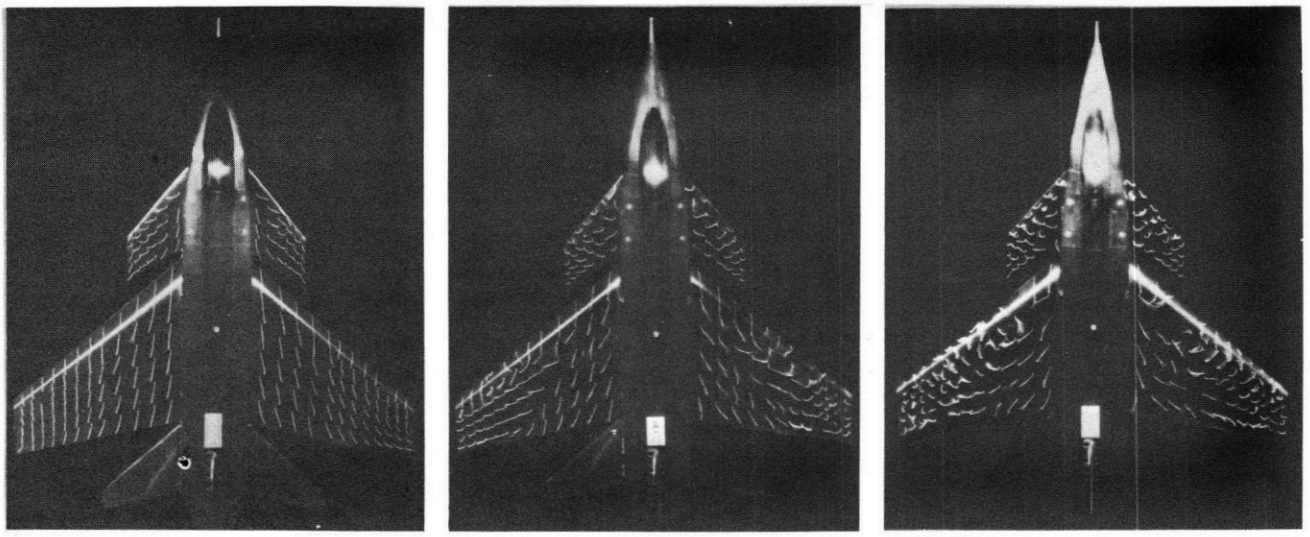

a. α = 16° b. α = 22° c. α = 36°

Fig 5 Wing flow variation with angle-of-attack. M = 0.2, $\Omega b/2V$ = 0.04

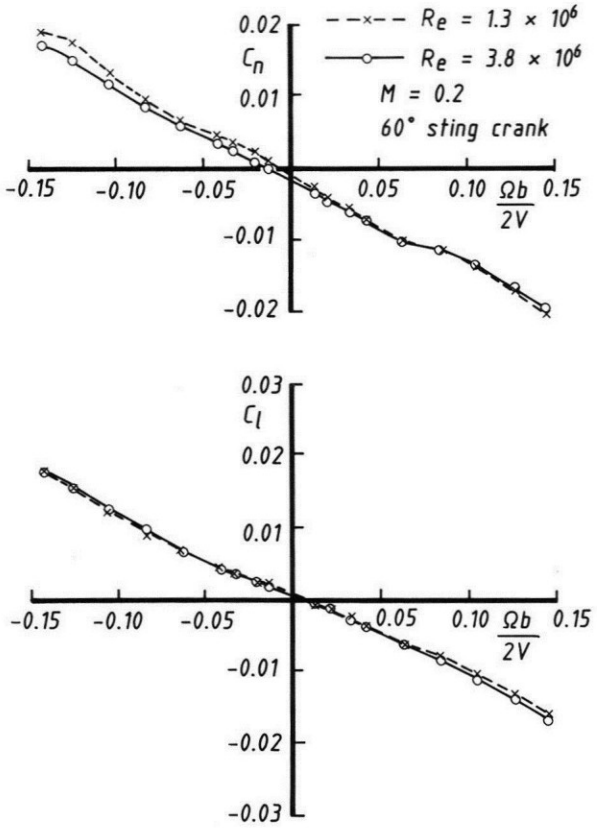

Fig 6a Reynolds number effects on C_n and C_ℓ. HIRM 2, α = 20°

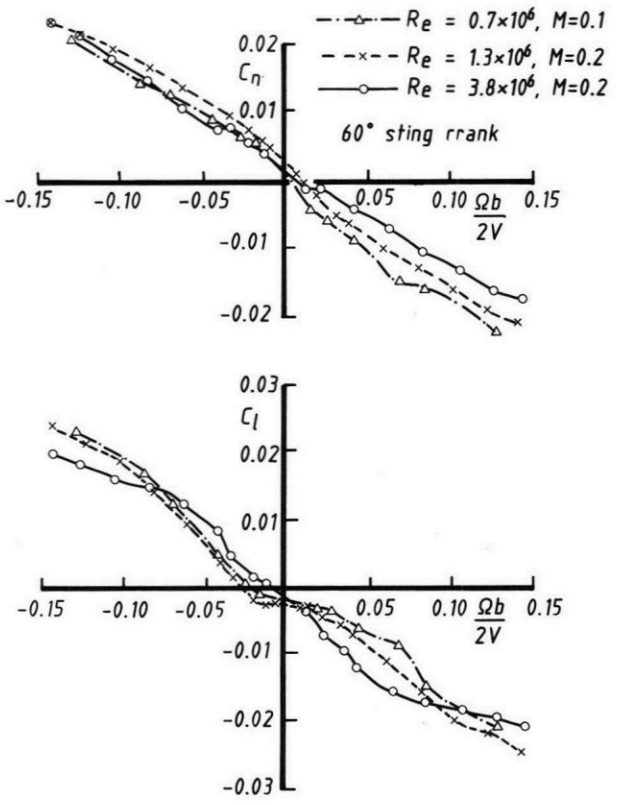

Fig 6b Reynolds number effects on C_n and C_ℓ. HIRM 2, α = 40°

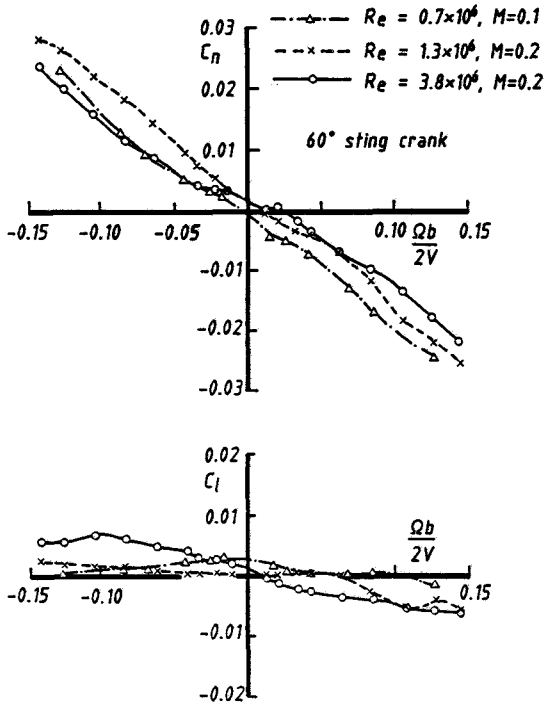

Fig 6c Reynolds number effects on C_n and C_ℓ.
HIRM 2, $\alpha = 50°$

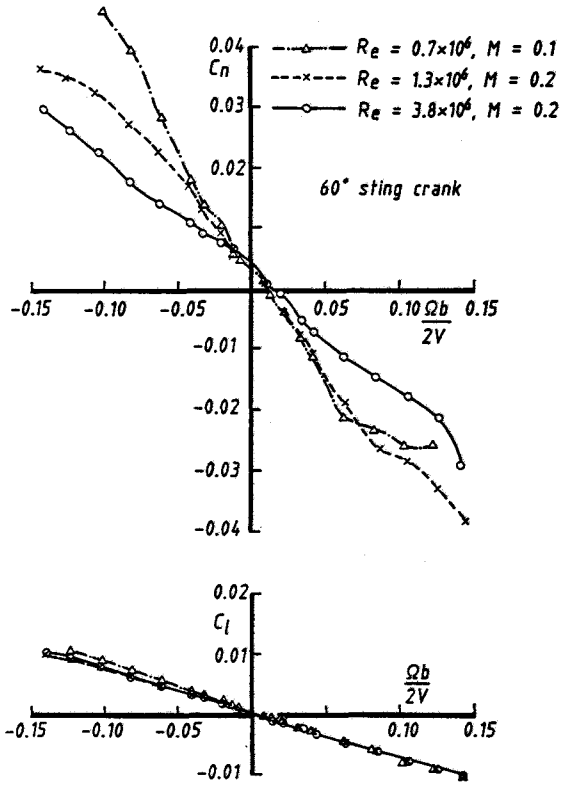

Fig 6d Reynolds number effects on C_n and C_ℓ.
HIRM 2, $\alpha = 60°$

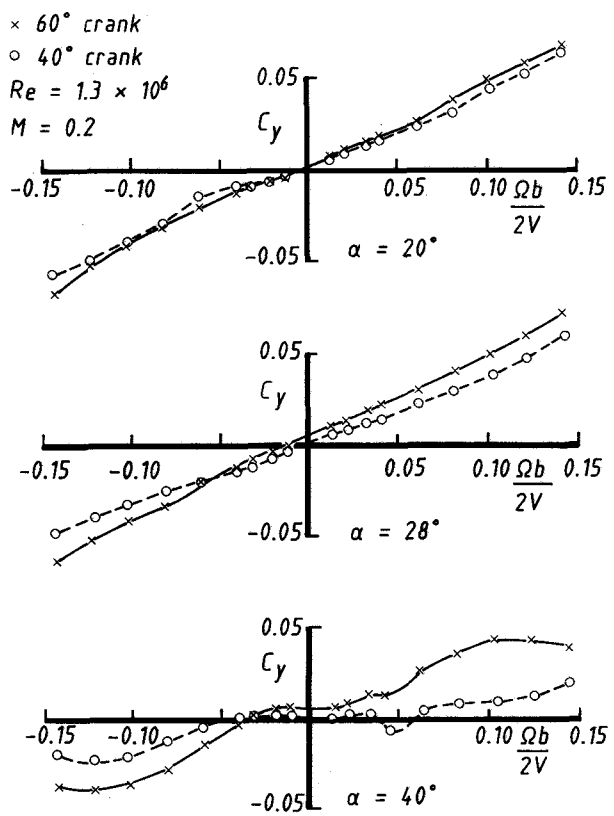

Fig 7a Effect of rear sting geometry on C_y.
HIRM 2

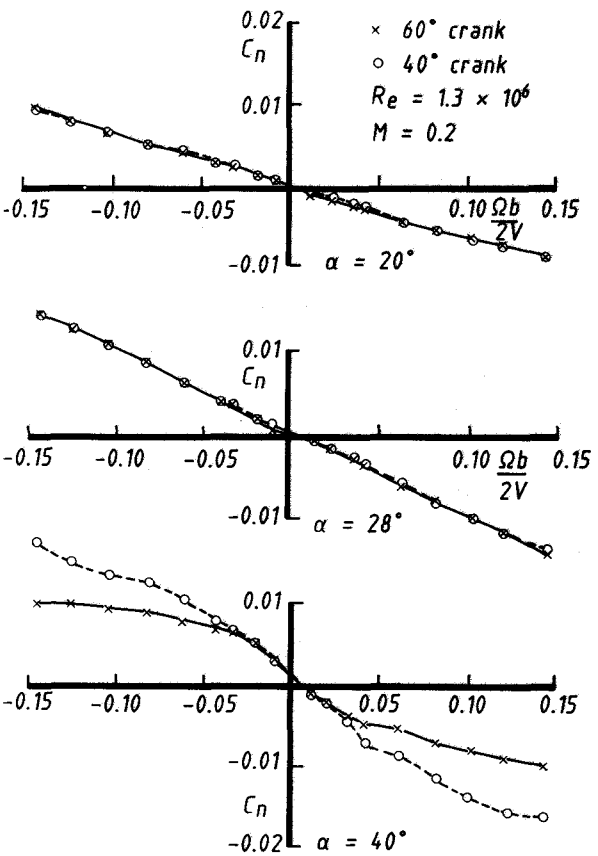

Fig 7b Effect of rear sting geometry on C_n.
HIRM 2

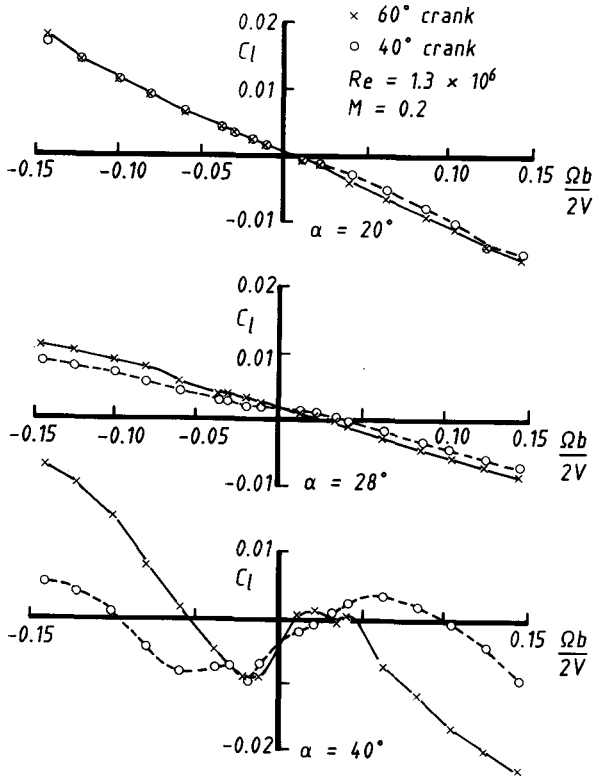

Fig 7c Effect of rear sting geometry on C_ℓ.
HIRM 2

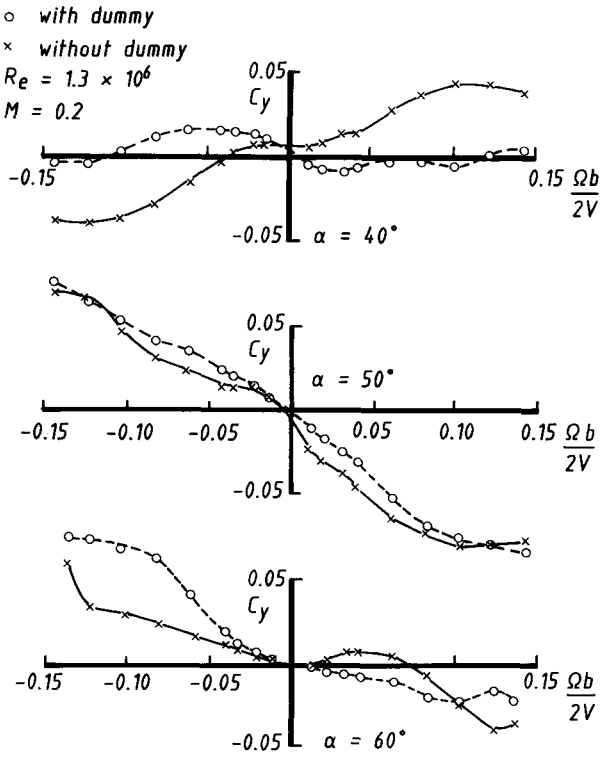

Fig 8a Effect of dummy top-entry sting on Cy.
HIRM 2

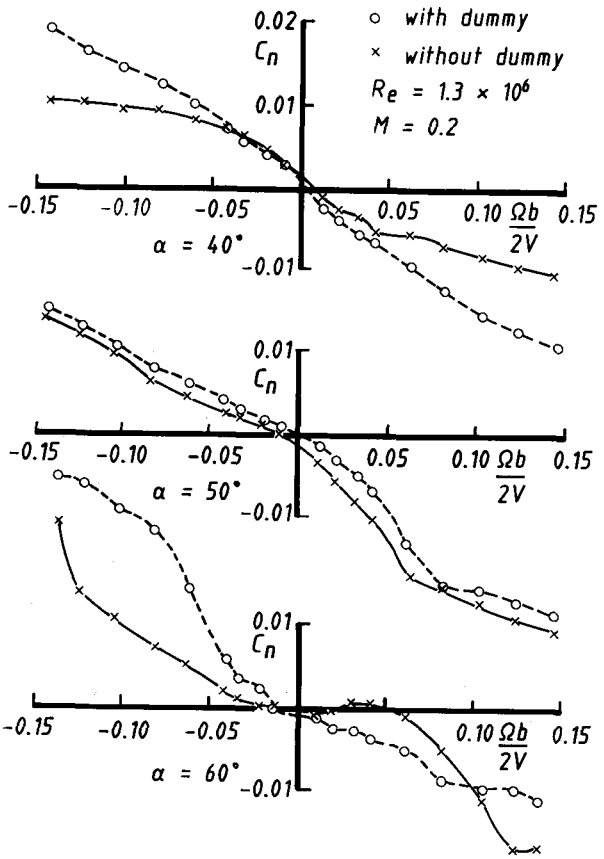

Fig 8b Effect of top-entry sting on C_n.
HIRM 2

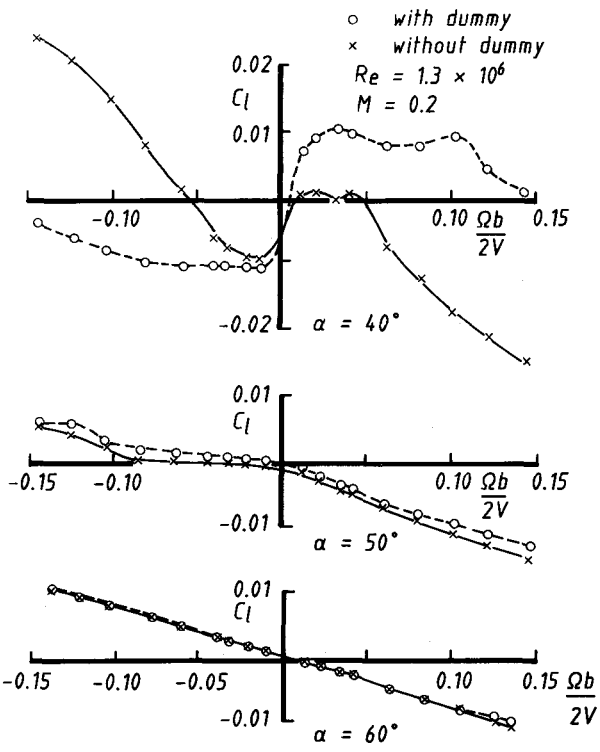

Fig 8c Effect of dummy top-entry sting on C_ℓ.
HIRM 2

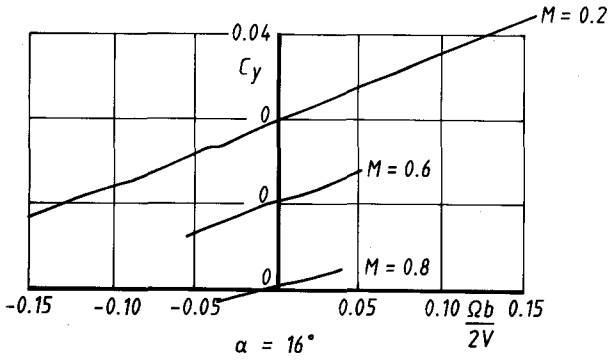

R_e = 1.3 × 10^6, 40° sting crank

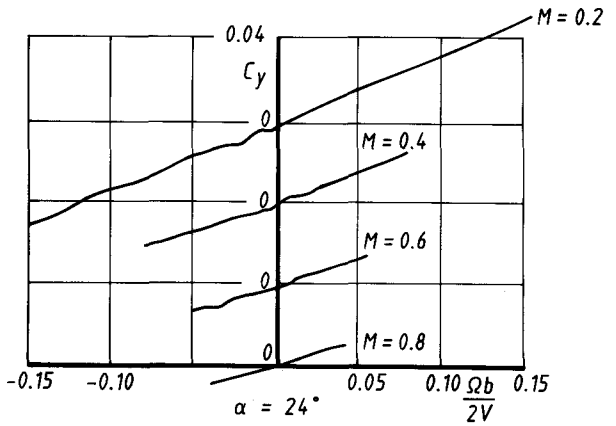

Fig 9a Mach number effects on Cy.
HIRM 2

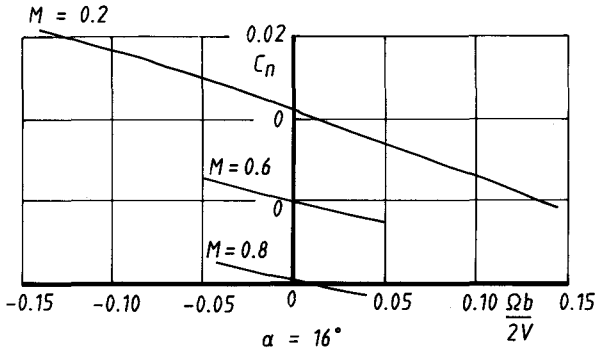

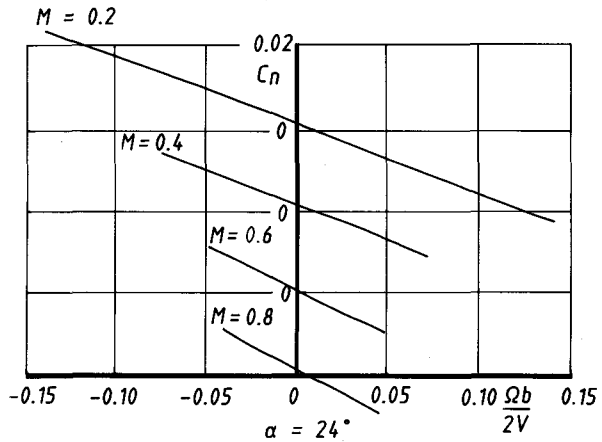

Fig 9b Mach number effect on C_n.
HIRM 2

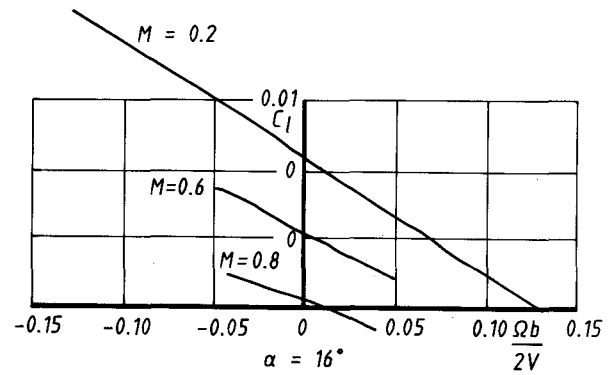

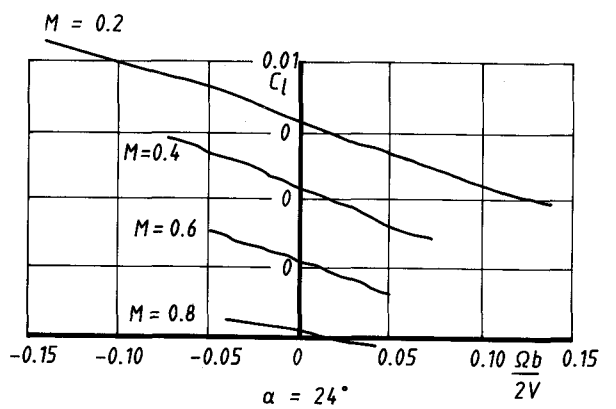

Fig 9c Mach number effects on C_ℓ.
HIRM 2

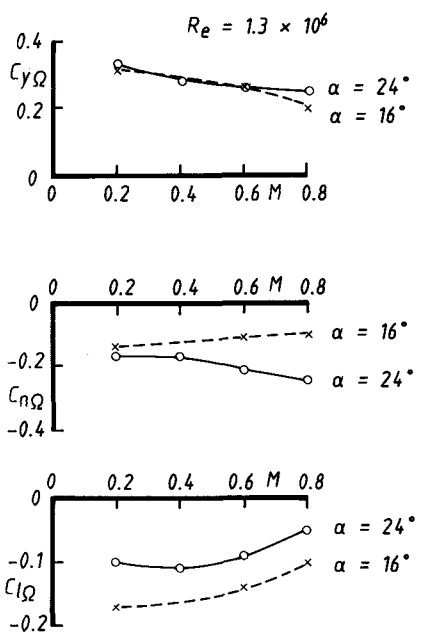

Fig 10 Mach number effects on derivatives.
HIRM 2